Lawrence Berkeley Laboratory

UNIVERSITY OF CALIFORNIA

IMAGING PROPERTIES OF A POSITRON TOMOGRAPH
WITH 280 BGO CRYSTALS

Stephen E. Derenzo, Thomas F. Budinger,
Ronald H. Huesman, John L. Cahoon, and
Tony Vuletich

November 1980

Biology &
Medicine
Division

IMAGING PROPERTIES OF A POSITRON TOMOGRAPH
WITH 280 BGO CRYSTALS

Stephen E. Derenzo, Thomas F. Budinger, Ronald H. Huesman,
John L. Cahoon, and Tony Vuletich

Donner Laboratory and the Lawrence Berkeley Laboratory
University of California
Berkeley CA, 94720

Summary

The basic imaging properties of the Donner 280-BGO-Crystal positron tomograph
were measured and compared with the same system when it was equipped with 280
NaI(Tl) crystals. The NaI(Tl) crystals were 8 mm X 30 mm X 50 mm deep, sealed in
10 mm wide stainless steel cans. The BGO crystals are 9.5 mm X 32 mm X 32 mm deep
and as they are not hygroscopic do not require sealed cans. With a shielding gap of
3 cm (section thickness 1.7 cm FWHM) the sensitivity of the BGO system is 55,000
events per sec for 1 μCi per cm^3 in a 20 cm cylinder of water, which is 2.3 times
higher than the NaI(Tl) system. For a 200 μCi/cm line source or the ring axis in a
20 cm diameter water cylinder, the BGO system records 86% of the scatter fraction
and 66% of the accidental fraction of the NaI(Tl) system. The lower light yield and
poorer time resolution of BGO requires a wider coincidence timing window than
NaI(Tl). However, the ability to use full-energy pulse height selection with a
2.3-fold improvement in sensitivity results in an overall reduction in the fraction
of accidental events recorded. The in-plane resolution of the BGO system is 9-10 mm
FWHM within the central 30 cm diameter field, and the radial elongation at the edge
of the field in the NaI(Tl) system has been nearly eliminated.

1. Introduction

The combination of radionuclide tracer techniques and computed tomography has
the unique ability to quantitate the amount of tracer in well-defined regions of the
body and thereby provide the functional or metabolic activity in vivo as a function
of time. The history of this field over the past 18 years has been described in
several review articles. [1-3]

The design objective of our instrumentation at Donner Laboratory is to achieve
high resolution, gated, dynamic imaging with minimum mechanical motion. We have
previously described the properties of the Donner 280-crystal positron tomograph
with NaI(Tl) scintillation crystals. [4-7] Recently the NaI(Tl) crystals have been
replaced with bismuth germanate (BGO) scintillation crystals and this has given us
the unique opportunity to compare these two detector materials in a large positron
imaging system.

In this paper we describe the imaging properties of the Donner 280-BGO-Crystal
Tomograph and compare these to the NaI(Tl) detector system.

2. System Description

2.1 Overall Organization

As described in Refs. 4-6, each detector is in time coincidence with 105 opposing detectors, providing 14,700 projection measurements of the positron activity distribution in the 50 cm diameter patient port. These data are reorganized into 140 projection angles (1.29^0 spacing) of 105 parallel rays (5.3 mm average spacing). The 196 cm diameter gantry contains 280 detector assemblies, preamplifiers, and discriminators as well as movable lead shielding for the selection of section thickness and a remotely controllable hoop source of ^{68}Ge for transmission measurements (Fig. 1). The detector assemblies (crystal, lightpipe, and phototube) are mounted in groups of five on a "U"-shaped aluminum frame that can be removed from the gantry as a unit. See Table 1 for a general summary of system parameters.

2.2 Detectors

Fig. 2 shows one of the 280 detector assemblies with its BGO crystal, quartz lightpipe, and 38 mm diameter phototube. In our experience, MgO is a better reflector than TiO_2 paint, aluminum foil, or millipore filter paper. Consequently, we first spray the crystals with MgO in water suspension. After drying, they are sprayed with TiO_2 paint to provide a more durable coating. Each assembly is then wrapped with aluminum foil and black tape. The foil prevents the tape adhesive from being absorbed by the reflective coatings.

2.3 Electronics

A small printed circuit card, mounted near each phototube, contains a preamplifier and two leading edge discriminators. The phototube full-energy pulses (511 keV) typically produce a 30 mV signal when driving a 1,000 ohm load. The preamplifier provides 300 mV signals (10X gain) to the two discriminators. The lower discriminator (30 mV or 50 keV) establishes an accurate timing pulse, and the higher discriminator (150 mV or 250 keV) is used to reject phototube noise pulses and annihilation photons that have scattered through large angles (typically >90^0).

The 560 digital discriminator signals are sent to a separate electronics rack where they are organized into 35 groups of eight detector channels. Each group of eight is placed in coincidence with the 14 opposing groups of eight. Thirty-five coincidence gates are used to determine the on-time (image + scattered + accidental) coincidences and 35 other gates determine the off-time (accidental) coincidences. The full time window for all gates is 25 nsec.

Additional circuits determine the addresses of the two crystals whenever a coincidence occurs. An event is rejected if more than one crystal or more than one group of eight crystals is involved on either side of the ring.

Table 1. The Donner 280-Crystal Positron Tomograph

Crystal Material[a]	NaI(Tl)	$Bi_4Ge_3O_{12}$ (BGO)
Density (gm/cm^3)	3.67	7.13
Atomic Numbers	11, 53	83, 32, 8
Crystal Size (mm)	8 X 30 X 50 deep	9.5 X 32 X 32 deep
Crystal Spacing (center-to-center)	10.3 mm	10.5 mm
Diameter of Detector Ring	92 cm	94 cm
Patient Port Diameter	50 cm	50 cm
Shielding Depth	21 cm	22 cm
Section Thickness[b]	17 mm FWHM at center	17 mm FWHM at center
Time Resolution	9 nsec FWHM 18 nsec FW(0.1)M	15 nsec FWHM 30 nsec FW(0.1)M
Lower Discriminator	10 keV	50 keV
Upper Discriminator	100 keV	250 keV
Detection Efficiency at 511 keV[c]	45%	67%
In Plane Resolution (FWHM)[d]	7 mm at center 9 mm at 10 cm	7 mm at center 9 mm at 10 cm

[a]NaI(Tl) from Bicron Corp., 12345 Kinsman Rd., Newbury OH 44065
 BGO from Crystal Technology Inc., 1035 East Meadow Circle, Palo Alto CA 94303
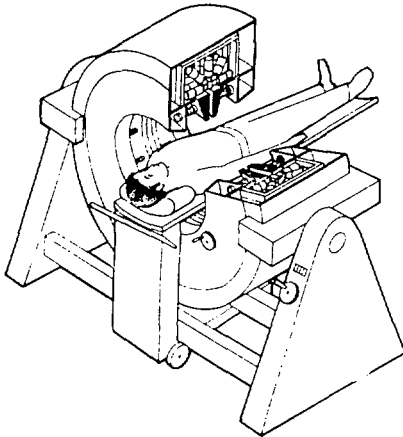[b]Adjustable from 1 to 17 mm
[c]Upper discriminator pulses from one crystal only.
[d]Depends on positron energy and reconstruction filter. See Table 4.
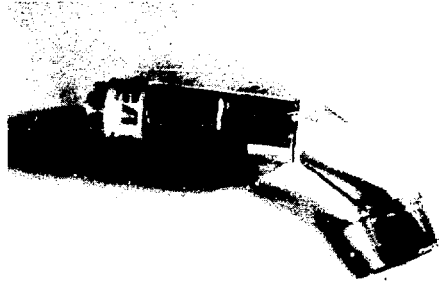
2.4 Data Accumulation and Reconstruction

This portion of the system (described in Ref. 7) is briefly summarized below:

The events are accumulated in a CMOS semiconductor memory system consisting of eight circuit boards with 14,700 words each. Each word has 12 bits for data and one bit for parity. A deadtime of 1 usec is required to: (1) receive the two crystal addresses, (2) calculate a parallel ray coordinate, (3) read the appropriate word from memory, (4) increment (or decrement) the word, and (5) write the word back into

Figure 2: Detector assembly, consisting of a rectangular BGO crystal 9.5 mm x 32 mm x 32 mm deep, quartz lightpipe and 38 mm diam photomultiplier tube. Assembly is coated with MgO reflector and Ti_2 paint before wrapping with aluminum foil and black tape.

CBB800-12359

XBL812-3648

Figure 1: Schematic of Donner 280-BGO-Crystal Positron Tomograph.

memory. On-time events cause the memory word to be incremented, and off-time events cause the word to be decremented. The accidental background is subtracted in this way.

The hard-wired memory system allows data acquisition on one board while simultaneously transferring data to disc from another board, using a DEC-11/34 minicomputer for data routing and a DEC RK-05 removable disc cartridge drive for storage. This feature permits up to eighty sequential images as short as 2 sec each to be taken for rapid sequence studies. Alternatively, for gated heart studies, data are accumulated in the eight memory boards corresponding to selected intervals of the cardiac cycle. At the conclusion of the study, data from each of the memory boards are transferred to disc storage. Gated sequential studies with a maximum of four gating intervals are also possible.

2.5 Image Display and Analysis

Reconstructed images are displayed using a DeAnza[8] image display system with 256 X 256 by 12 bit refresh memory. Regions of interest are drawn with a joystick, and the reconstructed intensity within each region (and for each sequential image) is written to a disc file for input to kinetic model fitting programs.

3. Imaging Properties

3.1 Event Rates

In Table 2 we list measured rates for a 20 cm diameter, 20 cm high cylinder of water containing approximately 0.2 μCi/cm^3 of ^{68}Ga (positron yield 89%).

Table 2. Rates for 1 μCi/cm^3 in a 20 cm Diam Cylinder of Water

	BGO[a]			NaI(Tl)[b]		
Shielding Gap (mm)	10	20	30	10	20	30
System Singles Rate (10^3/sec)	455	1,505	2,625	403	1,418	2,415
Total Coincident Event Rate[c]	8,890	43,000	103,000	2,700	19,400	47,300
Image Plus Scattered Coincidences (per sec)[d]	6,770 (76%)	26,000 (60%)	55,000 (53%)	2,200 (81%)	11,800 (61%)	24,000 (51%)
Accidental Coincidences (per sec)	2,120 (24%)	17,000 (40%)	48,000 (47%)	500 (19%)	7,600 (39%)	23,300 (49%)

[a]Measured using approximately 0.2 μCi/cm^3 of ^{68}Ge and converted to 1 μCi/cm^3 of pure positron emitter. Minor corrections for 2.5 usec system deadtime were also made.
[b]From Ref 6, after corrections for deadtime
[c]Total number of events in the on-time coincidence window
[d]Determined by subtracting the off-time events (accidental coincidences) from the on-time events (image + scatter + accidental coincidences).

Although the singles rates are only slightly higher for BGO than for NaI(Tl), the image plus scattered coincidences (i.e. those in true time coincidence) for BGO are larger than those for NaI(Tl) by a factor of 2.3.

Table 3 shows measured rates for a 200 μCi/cm line source on the ring axis, both in air and at the center of a 20 cm diameter water cylinder, and for the BGO and the NaI(Tl) systems. The data were taken using a 1.4 cm diameter, 14 cm long tube containing approximately 2 mCi of ^{68}Ge; and all rates were converted to 200 μCi/cm of pure positron emitter in air. Since the source occupied only a small portion of the field, we can separate the image events (unscattered annihilation pairs that pass through the source) from the scattered events (where both photons are from the same positron but one or both have scattered in the water or in the side shielding). The accidental event rate (chance coincidences of unrelated photons) is determined from the events collected in the off-time coincidence window. As expected, both the scatter and accidental fractions are improved by reducing the shielding gap but at a great sacrifice in sensitivity[4]. With the line source in air, the scattered events arise from scattering in the lead shielding.

Table 3. Rates for a 200 μCi/cm Line Source on the Ring Axis[a]

Shielding Gap (mm)	BGO			NaI(Tl)		
	10	20	30	10	20	30
IN AIR:						
System Singles Rate (10^3 per sec)	354	1,173	1,957	406	1,190	2,030
Total Recorded Event Rate[b]	18,900	64,600	109,400	7,800	31,800	57,000
Image Fraction[c]	92%	85%	81%	90%	83%	77%
Scatter Fraction[d]	4%	5%	5%	3%	5%	5%
Accidental Fraction	5%	10%	14%	6%	12%	18%
Reconstructed events (50 cm field)[e]:						
Image Fraction[c]	95%	93%	92%	95%	93%	92%
Scatter Fraction[d]	4.9%	6.6%	7.8%	5.1%	6.5%	7.6%
Reconstructed events (30 cm field)[e]:						
Image Fraction[c]	97%	96%	95%	95%	95%	94%
Scatter Fraction[d]	3.4%	4.4%	5.5%	4.6%	5.2%	6.1%
IN 20 CM DIAM WATER CYLINDER:						
System Singles Rate (10^3 per sec)	245	795	1,330	364	1,110	1,925
Total Recorded Event Rate[b]	3,500	15,100	30,500	1,850	10,300	24,100
Image Fraction[c]	74%	59%	51%	63%	45%	34%
Scatter Fraction[d]	10%	14%	15%	13%	16%	16%
Accidental Fraction	15%	26%	34%	24%	39%	50%
Reconstructed Events (50 cm field)[e]:						
Image Fraction[c]	93%	88%	86%	89%	84%	81%
Scatter Fraction[d]	7.0%	11.8%	14%	10.5%	15.6%	19%
Reconstructed Events (30 cm field)[e]:						
Image Fraction[c]	94%	90%	88%	91%	86%	83%
Scatter Fraction[d]	6.2%	10.4%	12%	9.3%	13.6%	17%

[a]Data taken using approximately 200 μCi/cm of ^{68}Ge and converted to 200 μCi/cm of pure positron emitter. Deadtime corrections (approximately 25% loss at 100,000 events per sec) not made for BGO data or NaI(Tl) data (Ref. 6).
[b]Total rate (per sec) for the on-time coincidence window. In addition, an independent sample of accidental events is recorded in the off-time window.
[c]Events within 25 mm of the line source.
[d]Events farther than 25 mm from the line source (i.e. coincident scatter background).
[e]After accidental background subtraction, attenuation correction, and reconstruction.

Fig. 3 shows the imaging response of the system to a 1.2 mm diameter ^{68}Ge line source moved from the ring center to a radius of 22.5 cm in 2.5 cm steps. The projection data were added before reconstruction.

The sensitivities of the two systems for a line source in air are plotted in Fig. 4 as a function of the distance from the source to the ring axis. The greater sensitivity of the BGO system relative to the NaI(Tl) system is clearly shown, and the sensitivity is greater near the edge of the field for both systems because on the average the coincident crystals are closer to the source and the solid angle is larger.

3.2 In-plane Resolution

Precision measurements of the width of the reconstructed point spread function (PSF) as a function of the distance to the ring center are plotted in Figs. 5 and 6. The PSF is sharpest at the exact center having 6.9 mm FWHM and 13.4 mm FW(0.1)M. As the source is moved outward from the ring center, the PSF undergoes changes in shape with an approximate 5.3 mm periodicity that reflects the way that the stationary ring system samples the object space.[3,4]

In the central region of the imaging field, there is no significant difference in resolution between the BGO and NaI(Tl) systems. At the edge of the field, however, the radial resolution of the BGO detectors is clearly superior to that of the NaI(Tl) detectors due to the reduction in side penetration. In Table 4, we list the resolution widths as a function of the distance from the line source to the ring axis for both the BGO and NaI(Tl) systems; for ^{22}Na and ^{68}Ge; and for two different reconstruction filters. The positron range smearing for ^{22}Na is less than that of ^{68}Ge. Thus, the measured resolution is somewhat better. The reconstruction filter also effects the resolution, and the Ramachandran-Lakshminarayanan filter[9] provides somewhat better resolution than the Shepp-Logan filter[10] used for most of this work.

3.3 Z-axis Resolution

To measure the effectiveness of the lead shielding in blocking annihilation photons originating from activity outside the section being imaged, we measured the system response to a small source in a 20 cm diam, 20 cm long water cylinder as it was moved along the ring axis. The ^{68}Ge source was 30 mm in diameter and 5 mm thick, set parallel to the plane of the ring. The relative rates of image, scattered, and accidental events are plotted in Fig. 7 for a 20 mm shielding gap. Table 5 shows the axial resolution widths for 20 mm and 30 mm shielding gaps. See Ref. 4 for similar measurements taken with opposing groups of NaI(Tl) detectors.

3.4 Phantom Images

Fig 8 shows images of a test phantom consisting of a solid lucite cylinder 20 cm in diameter and 7.5 cm high with triangular arrays of holes of diameters 2.5, 3, 3.5, 4, 5, and 6.25 mm and center-to-center spacings of 10, 12, 14, 16, 20, and 25 mm, respectively.

XBB800-12430

Distance from source to ring axis (cm)

XBL8010-3787
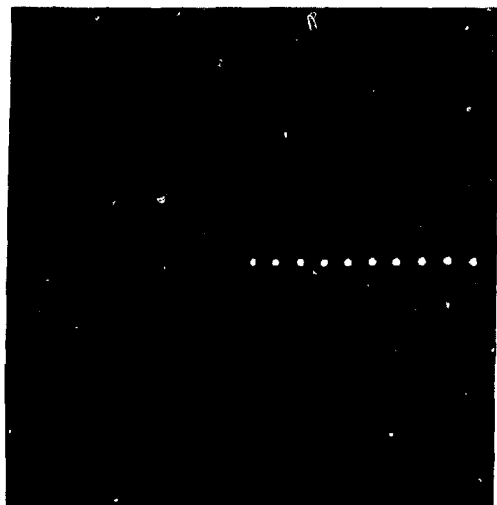
Figure 3: Image of a 1.2 mm diam line source of Na^{22} moved from the ring axis to a radius of 22.5 cm in 2.5 cm steps Projection data were added before reconstruction. Note the lack of radial elongation that is seen with NaI(Tl) detectors (Refs. 4,6)
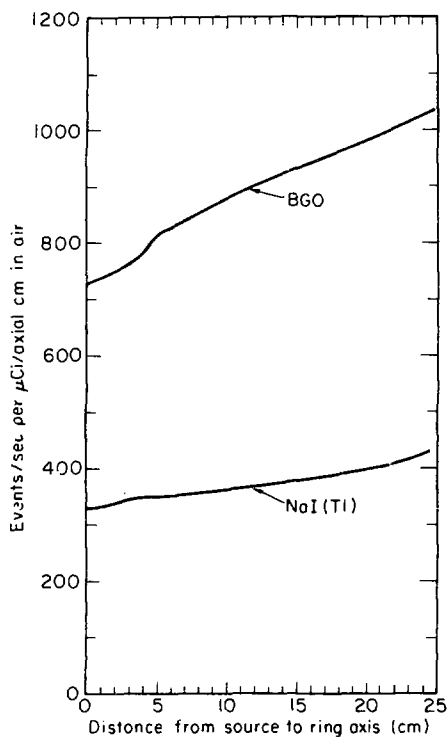
Figure 4: Sensitivity of the NaI(Tl) and BGO systems for a line source in air parallel to the ring axis.

The phantom was imaged with ^{18}F (0.64 MeV max), ^{68}Ga (1.90 MeV max), and ^{82}Sr-^{82}Rb (3.35 MeV max). Although the resolution of the ^{82}Sr image is poorest, the primary effect of the greater positron energy is the reduction in contrast, due to the extensive tails of the range distribution (as described in Ref. 11).
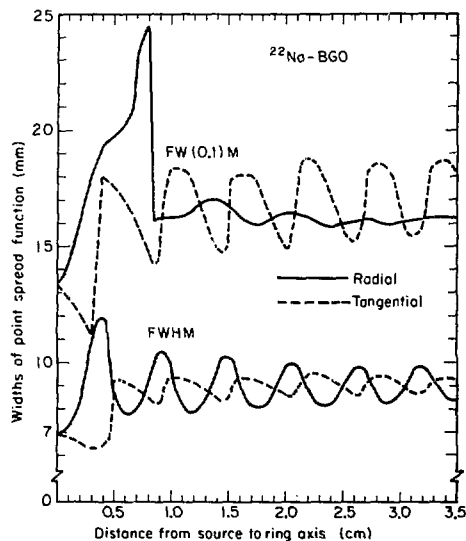
XBL8010-3783

Figure 5: Widths of the radial and tangential profiles of the reconstructed image of a ^{22}Na point source in air as a function of the distance to the ring center. Source was 1.2 mm diam in a 13 mm diam lucite cylinder to stop all positrons. Undulations have a periodicity of 5.3 mm and correspond to the way the stationary ring samples the object space. The undulations are strongest in the central region of the imaging field.
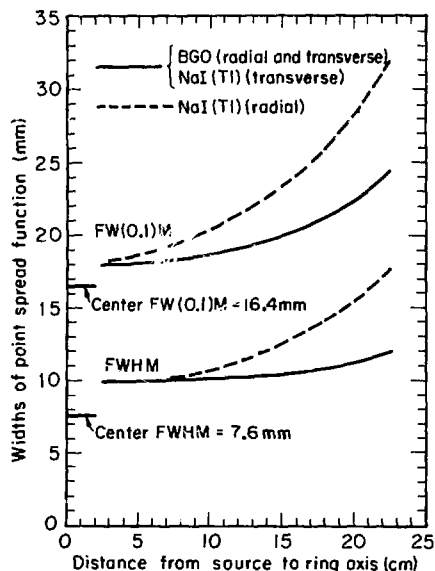
XBL8010-3782

Figure 6: Widths of the radial and tangential profiles of the reconstructed image of a ^{68}Ge point source in air as a function of distance to the ring center, averaged over fluctuations shown in Fig. 2

-9-

Table 4. Radial and Tangential Resolutions for Different
Detectors, Isotopes, and Reconstruction Filters

Detectors: Isotope: Max Energy: Filter:	BGO ^{22}Na 0.54 MeV RALA[b]		BGO ^{22}Na 0.54 MeV SHLO[c]		BGO ^{68}Ge 1.90 MeV SHLO[c]		NaI(Tl)[a] ^{68}Ge 1.90 MeV SHLO[c]	
	FWHM	FW(.1)M	FWHM	FW(.1)M	FWHM	FW(.1)M	FWHM	FW(.1)M
R= 0.0cm Radial	6.5	11.8	6.9	13.4	7.7	16.6	7.5	16.2
Tangential	6.5	11.8	6.9	13.4	7.7	16.6	7.5	16.2
R= 0.5cm Radial	8.2	19.2	8.7	19.6	9.1	20.4	9.4	20.2
Tangential	8.8	16.5	9.3	17.3	9.9	17.8	9.9	18.2
R= 1.0cm Radial	8.9	15.3	9.5	16.2	9.3	17.6	9.8	17.4
Tangential	8.8	17.2	9.3	18.3	10.0	19.1	9.8	19.3
R= 2.5cm Radial	8.3	14.6	9.0	15.9	10.3	17.6	10.8	18.8
Tangential	8.4	15.1	8.9	15.8	9.7	17.4	9.5	17.4
R= 5.0cm Radial	8.3	14.8	8.8	16.0	9.5	17.8	9.8	18.5
Tangential	8.9	17.4	9.4	18.6	10.3	20.0	9.8	18.5
R= 7.5cm Radial	8.9	14.9	9.4	16.0	10.4	17.8	10.1	19.2
Tangential	8.5	15.1	9.1	16.5	10.0	18.5	9.9	18.7
R=10.0cm Radial	8.4	15.2	9.0	16.5	9.8	18.0	10.7	20.4
Tangential	9.1	18.2	9.6	19.3	10.5	20.8	9.9	19.1
R=12.5cm Radial	9.4	15.9	9.8	17.1	10.7	18.8	11.3	21.7
Tangential	8.9	16.3	9.5	17.7	10.4	19.4	10.0	19.6
R=15.0cm Radial	8.9	16.7	9.5	17.8	10.5	19.3	12.5	23.3
Tangential	9.2	17.9	9.8	19.2	10.6	20.4	10.2	20.0
R=17.5cm Radial	9.2	18.1	9.8	18.9	10.9	20.6	13.8	25.3
Tangential	9.6	19.1	10.1	20.3	11.0	21.7	10.6	20.9
R=20.0cm Radial	10.0	20.0	10.6	20.7	11.4	22.1	15.4	28.3
Tangential	10.0	20.1	10.6	21.2	11.3	22.1	11.0	22.8
R=22.5cm Radial	11.2	22.6	11.6	23.2	12.4	24.7	17.6	31.8
Tangential	10.6	21.1	11.2	22.2	12.1	23.6	11.5	25.0

[a]Data from ref 6.
[b]Reconstruction filter from Ref. 9
[c]Reconstruction filter from Ref. 10

Figure 7: Z-axis response of the BGO system to a point source moving along the ring axis in a 20 cm cylinder of water. Shielding gap 2.0 cm.
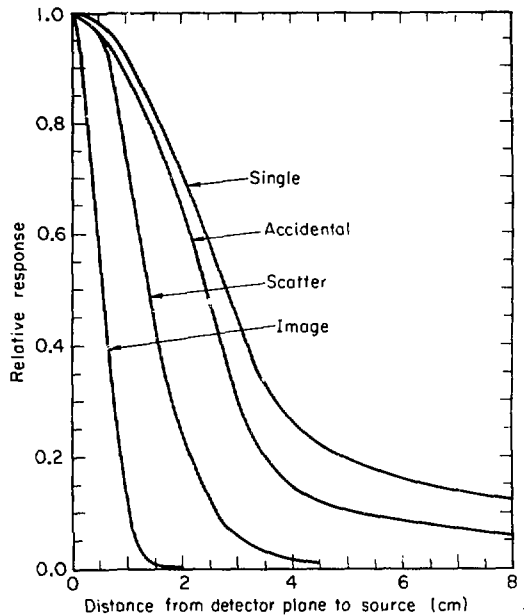
XBL8010-3786

Table 5. Z Axis Resolution[a] (BGO Detectors)

Shielding Gap:	20 mm	30 mm
Image Events:		
FWHM	11.5 mm	17.2 mm
FW(0.1)M	21 mm	29 mm
Scatter Events:		
FWHM	28 mm	38 mm
FW(0.1)M	52 mm	69 mm
Accidental Events:		
FWHM	46 mm	57 mm
FW(0.1)M	80 mm	104 mm

[a]Widths of response to a source in a 20 cm water cylinder translated along the ring axis.
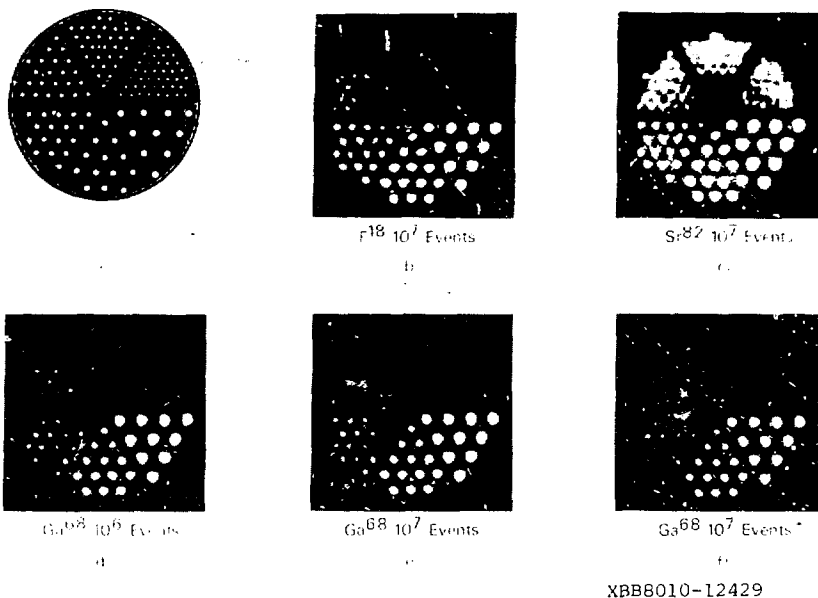
Figure 8: Images of a hot spot phantom using isotopes of different beta energies, different numbers of events, and different reconstruction filters.

4. Future Improvements

4.1 Improved Sampling

A stationary circular array with uniformly placed detectors performs a linear sampling with an average spacing of one-half the detector center-to-center spacing. The radial sampling pattern shown in Fig. 9a has concentric rings with this sampling distance. (The angular sampling for a stationary ring of closely spaced detectors is adequate.) The uniform sampling theorem implies that one cannot expect a resolution FWHM much better than the center-to-center distance between the detectors. To improve the linear sampling, various schemes for displacing the detector ring by small amounts (usually around a small circle) have been proposed; but all require sampling at many mechanical positions.[12-16] Other somewhat more complex motions of the non-wobble category have been presented but require more than two mechanical positions for a full sampling improvement at all angles.[17,18]
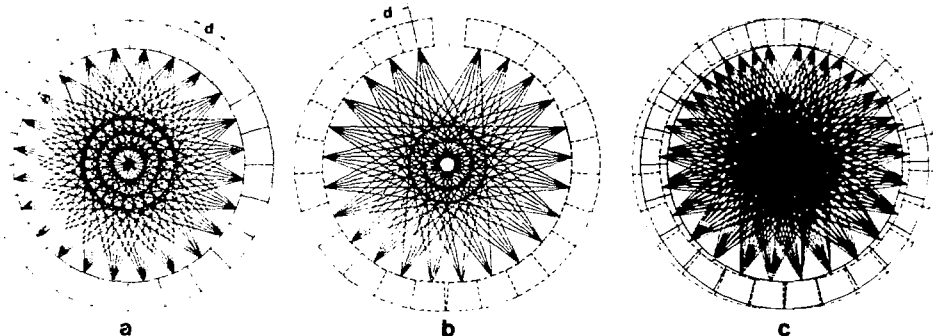
XBL802-3133

Figure 9: Improved linear sampling provided by "hinging" the detector array and opening the hinge like a clam shell to provide a one-crystal gap at the point opposite the hinge. In 9a, coincidence lines for all angles correspond to chords located at 0, $\pm d/2$, $\pm d$, etc. from the ring axis where d is the center-to-center crystal spacing. This may be seen in the "sampling rings" of radii 0, $d/2$, d, etc. that appear in a. For position b the coincidence lines form rings of radii $\pm d/4$, $\pm 3d/4$, etc. When both positions a and b are combined, the sampling rings have radii 0, $\pm d/4$, $\pm d/2$, $\pm 3d/4$, $\pm d$, etc. Thus, the linear sampling is improved by a factor of $\sqrt{2}$ at all angles with only two mechanical positions.

The implementation of these schemes would compromise our objective of rapid, gated, sequential imaging. However, we have discovered displacement schemes where only two mechanical positions provide a uniform doubling of the linear sampling frequency at all angles. One scheme involves moving the crystals circumferentially so that a gap the size of one crystal occurs. This transforms the array from an even to an odd number of detectors. A second method, which is an adequate approximation to the even-odd method, involves merely hinging the detector array and rotating each side (like a clam shell) to open up a space the size of one crystal at the point opposite the hinge (Fig. 9). Both methods involve mechanical displacement of precisely aligned crystal-phototube assemblies. Another implementation of this idea is a multi-ring system with alternating circular rings of even and odd numbers of crystals. The sampling is done by a two-position z-axis translation. The uniqueness of this design approach involves the recognition that an improved linear sampling can be accomplished with only two mechanical positions of the patient bed and a stationary multi-ring array.

4.2 Attenuation Correction Methods

The quantitative ability of positron tomography is greatly dependent on the ability to compensate for the photon attenuation. The compensation for variable attenuation situations, such as encountered in the human thorax, relies heavily on the acquisition of transmission data with good statistics. The Donner 280-crystal tomograph utilizes a continuous hoop source[6]; but, due to the accidental background, it is only possible to measure typically 40 events per minute per projection bin

-13-

through the equivalent of 20 cm of water, with an equal number of accidental events. This problem and the inconvenience of acquiring a transmission measurement have led investigators to estimate the attenuation coefficient distribution based on the object outline when a more or less constant distribution is expected, as in the head[19].

A method for acquisition of transmission data which is not limited by accidentals utilizes a rapidly moving line source with detection of a fan beam of data. Data are collected in a non-coincident mode in which the position of the source at any moment is known to be the origin of the fan. Another technique utilizes a moving positron line source operating in coincidence mode, but the accepted data are only those events that pass through the source. This is a significant improvement over the continuous positron hoop source, and the remaining limitation of both of these approaches is in crystal and discriminator deadtime.

4.3 Scatter Background Correction

One of the most important problems in positron tomography is the background noise from scattered coincidences. Depending on the instrument design, between 20% and 50% of the detected coincidences are actually unwanted scattered events in which the two photons detected in coincidence come from the same positron-electron annihilation. However, one or both photons scattered before arrival at the detector. Two methods to control the amount of background from scattered coincidences are shielding[20-22] and a posteriori image processing. We previously proposed two techniques for this computational correction of scattered backgrounds. The first requires using the reconstructed image as an estimate of the true source distribution and the transmission image as the distribution of scattering coefficients. The predicted scatter is calculated using the Klein-Nishina formula, the known scattering coefficients, and the detector geometry. A second general technique involves approximating the scatter distribution function by some convolution kernel which takes into account the long tails of the true distribution. The original image is folded with this function and a fraction of the resulting "scatter image" is subtracted from the original. The fraction is determined empirically or theoretically. Iterative refinements can be made with both approaches.

4.4 Multi-Layer System

Poor coupling between small crystals and phototubes is the major limitation of a high-resolution positron system design incorporating multiple layers of close-packed scintillation crystals in ring arrays. Many designs have been suggested ranging from light pipe arrangements to inefficient matching of commercially available cylindrical phototubes to square or circular crystals. However, the published designs become impractical when a resolution of 5 mm is desired in a multi-layer tomograph able to dynamically image the human thorax.

To accomplish this objective we propose the following schemes: (1) Direct coupling to specially fabricated square phototubes containing multiple electron multipliers and anodes. (2) Multiple crystal coupling to square single-anode phototubes with sense wires for position information (This technique was investigated by Charpak[23,24] and its use for this application was suggested to us by H.O. Anger in 1975). (3) Use of a phototube window with high index of refraction,

such as dense glass or BGO itself. This would permit much of the scintillation light usually trapped by total internal reflection to reach the photocathode.

Relative to the Donner 280-BGO-Crystal Tomograph, potential improvements of a factor of four in photoelectron yield, a factor of ten in positron sensitivity, and a factor of two in spatial resolution can be realized by an improved 5-layer system of 2000 crystals with alternating even and odd-crystal layers.

5. Conclusions

In our system, BGO has three primary advantages over NaI(Tl):

(1) A factor of 2.3 higher useful event rates for a given amount of activity,

(2) Reduced side penetration resulting in improved resolution in the outer regions of the imaging field, and

(3) Rejection of tissue-scattered annihilation photons by pulse height selection without significant loss in detection efficiency for the wanted unscattered photons. In spite of the lower scintillation yield of BGO, and a poorer timing resolution, there is an overall reduction in the fraction of accidental coincidences.

Acknowledgments

References

1. Phelps E: Emission Computed Tomography. Sem in Nucl Med 7: 337-365, 1977

2. Brownell GL, Correia JA, Zamenhof RG: Positron instrumentation. In Recent Advances in Nuclear Medicine, Lawrence JH and Budinger TF, eds., Vol 5, 1978, pp 1-50

3. Budinger TF, Derenzo SE, Gullberg GT, and Huesman RH: Trends and prospects for circular ring positron cameras. IEEE Trans Nucl Sci NS-26: No 2, 2742-2745, 1979

4. Derenzo SE, Budinger TF, Cahoon JL, Huesman RH, and Jackson HG: High resolution computed tomography of positron emitters. IEEE Trans Nucl Sci NS-24: No 1, 544-558, 1977

5. Derenzo SE, Banchero PG, Cahoon JL, Huesman RH, Vuletich T, and Budinger TF: Design and construction of the Donner 280-crystal positron ring for dynamic transverse section emission imaging. Proceedings of the IEEE Conference on

Decision and Control, IEEE 77CH1269-0CS, Vol 1, 1977

6. Derenzo SE, Budinger TF, Cahoon JL, Greenberg WL, Huesman RH, and Vuletich T: Tne Donner 280-crystal high resolution positron tomograph. IEEE Trans Nucl Sci NS-26: No 2, 2790-2793, 1979

7. Huesman RH and Cahoon JL: Data acquisition, reconstruction and display for the Donner 280-crystal positron tomograph. IEEE Trans Nucl Sci NS-27: No.1, 474-478, 1980

8. DeAnza Systems, Inc., 118 Charcot, San Jose, CA 95131

9. Shepp LA and Logan BF: The Fourier Reconstruction of a head section. IEEE Trans Nucl Sci NS-21: No 3, 21-43, 1974

10. Ramachandran GN and Lakshminarayanan AV: Three-dimensional reconstruction from radiographs and electron micrographs: application of convolutions instead of Fourier Transforms. Proc Nat Acad Sci US 68: 2236-2240, 1971

11. Derenzo S: Precision measurement of annihilation point spread distributions for medically important positron emitters. Proceedings 5th International Conference on Positron Annihilation, (Lake Yamanaka, Japan) pp 819-823, 1979

12. Eriksson L, Widen L, Bergstrom, et al: Evaluation of a high resolution ring detector positron camera. J Comput Assist Tomogr 2: 649, 1978.

13. Mullani NA, Ter-Pogossian MM, Higgins CS et al: Engineering aspects of PETT V. IEEE Trans Nucl Sci NS-26: No 2, 2703-2706, 1979

14. Brooks RA, Sank VJ, Talbert AJ, et al: Sampling requirements and detector motion for positron emission tomography. IEEE Trans Nucl Sci NS-26: No 2, 2760-2763, 1979

15. Herman GT: Data collection for cross-sectional image reconstruction by a moving ring of positron annihilation detectors. J Comput Assist Tomogr 3: 261-266, 1979

16. Huang SC, Hoffman EJ, Phelps ME, et al: Sampling requirements of emission computed tomographic (ECT) scanners. J Nucl Med 20: 609 (Abstract), 1979

17. Tanaka E, Nohara N, Yamamoto M, et al: "Positology" - the search for suitable detector arrangements for a positron ECT with continuous rotation. IEEE Trans Nucl Sci NS-26: No 2, 2728-2731, 1979

18. Hong KS: Oscillatory dichotomic ring positron camera. Multidimensional digital image processing- application to the 3-d image reconstruction, restoration, and enhancement, Cho ZH, Ed., Imaging System Science Laboratory, Korea Advanced Institute of Science, Seoul, Korea, 1979.

19. Huang SC, Hoffman EJ, Phelps ME, and Kuhl DE: Quantitation in positron emission computed tomography: 2. Effects of inaccurate attenuation correction. J Comput Assist Tomogr 3: 804-814, 1979

20. Derenzo SE, Zaklad H, and Budinger TF: Analytical study of a high- resolution positron ring detector system for transaxial reconstruction tomography. J Nucl Med 16: 1166-1173, 1975

21. Atkins FB, Harper PV, Scott R, et al: Analysis of coincident scatter for positron cameras using large area detectors. J Nucl Med 20: 635 (Abstract), 1979

22. Derenzo S: Method for optimizing side shielding in positron emission tomographs and for comparing detector materials. J Nucl Med 21: 971-977, 1980

23. Charpak G: The localization of the position of light impact on the photocathode of a photomultiplier. Nucl Instr Meth 48: 151-153, 1967

24. Charpak G: Retardation effects due to the localized application of electric fields on the photocathode of a photomultiplier. Nucl Instr Metn 51: 125-128, 1967